Catal Lett (2009) 127:132–142
DOI 10.1007/s10562-008-9656-5

SBA-15 as Support for Ni–MoS_2 HDS Catalysts Derived from Sulfur-containing Molybdenum and Nickel Complexes in the Reaction of HDS of DBT: An All Sulfide Route

Z.-D. Huang · W. Bensch · L. Kienle · S. Fuentes · G. Alonso · C. Ornelas

Received: 7 May 2008 / Accepted: 9 September 2008 / Published online: 3 October 2008

Abstract MoS_2 HDS catalysts promoted with Ni supported on SBA-15 were synthesized from sulfur containing Mo (ammonium thiomolybdate, ATM, and tetramethylammonium thiomolybdate, TMATM) and a Ni complex (Nickel diethylthiocarbamate, NiDETC). The catalysts have been characterized by X-ray diffraction (XRD), N_2-physisorption and High-resolution transmission electron microscopy (HRTEM). The catalytic performance in the hydrodesulfurization (HDS) reaction of dibenzothiophene (DBT) was examined at $T = 623$ K and $P_{H2} = 3.4$ Mpa. In comparison with the impregnation mode, the nature of the employed thiomolybdate complex shows a stronger influence on the MoS_2 morphology and consequently on the HDS activity of DBT. A similar high HDS activity to a commercial NiMo/γ–Al_2O_3 catalyst despite the pronounced stacking number is shown for a Ni–MoS_2/SBA-15 catalyst derived from ATM. The catalysts derived from TMATM showed lower HDS activities compared to the catalysts obtained from ATM precursors due to probably the presence of closed shell structures (nano-onions) of MoS_2 which offer significantly smaller amount of HDS active sites (edge sites). Moreover, the HYD/DDS ratios are interestingly higher with respect to the HYD/DDS ratio of the commercial NiMo/γ–Al_2O_3 catalyst which could be ascribed to the generation of multilayered MoS_2 active phase.

Keywords Hydrodesulfurization · (Alkyl)ammonium thiomolybdate · Nickel diethylthiocarbamate · Ni–MoS_2/SBA-15 HDS catalysts · HRTEM · MoS_2 morphology · Nano-onion · SBA-15 support

1 Introduction

It is a world-wide tendency that more stringent environmental regulations require the production of higher quality transportation fuels (gasoline, diesel) with lower sulfur concentration. It is a challenge to synthesize more active hydrodesulfurization (HDS) catalysts for the "deep refining" of crude oil to meet the new strict standards. Conventional γ–Al_2O_3-supported HDS catalysts are prepared using oxygen-containing transition-metal salts of Mo and W and of Co or Ni. The supported metal salt is calcined to produce stable oxidic materials that must be sulfided either prior to (ex situ) or during the start-up (in situ) of the hydrotreatment process. It is well known that for the conventional preparation of HDS catalysts via oxide routes, both calcination and sulfidation temperatures have a strong influence on the HDS activity. Incomplete sulfidation according to low sulfidation temperature or high calcination temperature leads to the decrease in HDS activity. Thus, alternate preparation procedures applying e.g. thiosalts in which sulfur is already bound to metal ions have been explored in the last several years.

Z.-D. Huang · W. Bensch (✉)
Institut für Anorganische Chemie, University of Kiel, Olshausenstraße 40-60, 24098 Kiel, Germany
e-mail: wbensch@ac.uni-kiel.de

L. Kienle
Max-Planck-Institut für Festkörperforschung, Heisenbergstr. 1, 70506 Stuttgart, Germany

S. Fuentes · G. Alonso
Universidad Nacional Autónoma de México, Centro de Nanociencias y Nanotecnología Ensenada, Mexico, DF B.C. C.P. 22860, Mexico

G. Alonso · C. Ornelas
Centro de Investigación en Materiales Avanzados S. C., Chihuahua C.P. 31109, Mexico

An attractive support material is the silica SBA-15 which has a large specific surface area and is more thermally stable than the related materials such as HMS or MCM-41 [1]. A high thermal stability is very important for applications in hydrotreating processes performed under the severe HDS reaction conditions like high temperatures and high H_2 partial pressures. Indeed, SBA-15 and hetero-atom containing (Al, Ti or Zr) SBA-15 were found to have excellent potential for deep hydrotreatment of petroleum feedstocks [2–7]. Very recently, CoMo sulfide catalysts supported on SBA-15 derived from ammonium thiomolybdate were reported by us [8, 9]. The catalysts activated in a H_2/N_2 (H_2 10%) gas flow showed a higher HDS activity compared to a commercial CoMo/γ–Al_2O_3 catalyst.

The aim of the present work is to study the catalytic behavior of NiMo catalysts supported on SBA-15 synthesized from pure sulfur precursors, e.g. S containing Mo (ammonium thiomolybdate, ATM, and tetramethylammonium thiomolybdate, TMATM) and Ni complexes (Nickel diethyldithiocarbamate, NiDETC) in the HDS reaction of DBT. In general, consecutive impregnation of SBA-15 support with Ni and Mo compounds was performed whereas first NiDETC was applied followed by the Mo sources ATM or TMATM. The preparation was also carried out with impregnation of SBA-15 material with NiDETC after the generation of (Ni)Mo sulfides. The different synthesis approaches should allow studying the effects of impregnation order onto the MoS_2 morphology and the HDS activity. The activation of the catalysts was carried out under H_2/N_2 (H_2 10%) gas flow avoiding any treatment in H_2S at high temperatures prior to the activity test. The catalysts are characterized with X-ray diffractometry (XRD), N_2 physisorption measurements using the Brunauer, Emmett and Teller (BET) method and high-resolution transmission electron microscopy (HRTEM). The catalytic HDS performance was tested with DBT in a batch reactor at 623 K with a H_2 pressure of 3.4 Mpa.

2 Experimental Section

2.1 Sample Preparation

2.1.1 Synthesis of Pristine Mesoporous SBA-15

The support material was prepared following the route published in [8–11].

2.1.2 Synthesis of Ni–MoS_2/SBA-15

2 g of SBA-15 (6 nm) was stirred for 4 h in 100 mL of saturated NiDETC chloroform solution at room temperature. NiDETC/SBA-15 was separated from the slurry by filtration and the obtained material was dried under vacuum over night. This material was then stirred in 150 mL of saturated aqueous solutions of ammonium thiomolybdate (ATM, at 298 K) or tetramethyl ammonium thiomolybdate (TMATM, at 328 K). The impregnation/activation cycle was carried out twice to prepare Ni–MoS_2/SBA-15 (6 nm) catalysts with higher Ni and Mo loading. After 4 h stirring the products were filtered without washing and then they were activated at 773 K for 3 h under a H_2/N_2 (H_2, 10%) gas flow at atmospheric pressure. For comparison purposes, two NiMo sulfide catalysts supported on 9 nm SBA-15 material were also prepared applying the same procedure. The catalysts will be designed according to their metal loading, type of synthesis procedure and type of SBA-15 support employed: Ni(X)Mo(Y)/SBA-15(PA) means the catalyst was prepared with ATM with X wt% Ni and Y wt% Mo loading and P is the pore size of SBA-15 in nm. Ni(X)Mo(Y)/SBA-15 (PB) is the abbreviation for the catalysts synthesized with TMATM.

Two additional samples were prepared by post-impregnation with NIDETC. The first one was prepared as follows: 2 g SBA-15 (6 nm) was stirred in 150 mL of saturated aqueous solutions of ATM at 298 K. After filtration the reaction product was calcined at 773 K for 3 h (H_2/N_2 (H_2, 10%) gas flow, atmospheric pressure). The calcined MoS_2/SBA-15 was treated with NiDETC chloroform solution, filtered and activated with the above mentioned conditions. The second catalyst was prepared to enhance the Ni concentration of Ni–MoS_2/SBA-15 catalysts. The Ni–MoS_2/SBA-15(6A) which was prepared by the above described synthesis method was treated in 100 mL of saturated NiDETC chloroform solution, and then the product was activated applying the above mentioned conditions. These two catalysts supported on 6 nm SBA-15 are denoted as Ni(X)Mo(Y)/SBA-15(6C) with X wt% Ni and Y wt% Mo loading.

The two Mo sources ATM and TMATM were synthesized with the same method reported previously [12] and the preparation of NiDETC has been published by Jorgensen [13].

2.2 Sample Characterization

X-ray diffraction (XRD) patterns were measured on a Siemens D5000 diffractometer at room temperature using CuKα radiation ($\lambda = 0.154056$ nm). Nitrogen adsorption measurements were carried out at 77 K on a Quantachrom Autosorb-1. Samples were degassed under flowing argon at 473 K for 2 h before N_2 adsorption. The BET surface areas were calculated from $p/p_0 = 0.03$–0.3 in the adsorption branch. The chemical composition of the catalysts (in wt%, average of five measurements at different points of the sample) was determined with energy dispersive X-ray

spectroscopy (EDS) analysis with a Philips ESEM XL 30 microscope.

The supported catalysts were analyzed by high resolution transmission electron microscopy (HRTEM) with a Philips CM 30ST microscope (LaB_6 cathode, 300 kV, $C_S = 1.15$ mm). The samples were grinded and suspended in n-butanol. One drop of each suspension was placed on a perforated carbon-copper net which serves as support of the particles. SAED (selected area electron diffraction) was carried out using a diaphragm which limited the diffraction to a circular area of 2,500 Å in diameter. All images were recorded with a Gatan Multiscan CCD camera and evaluated (including Fourier filtering) with the programs Digital Micrograph 3.6.1 (Gatan) or Crisp (Calidris). Chemical analyses by EDS were done in the nanoprobe mode or by spectral imaging (scanning mode) with a Si/Li detector (Noran, Vantage System). The device "Spinning Star" (NanoMEGAS) was applied for precession electron diffraction (PED, precession angle: 3°), simulated patterns were obtained via the software Emaps [14].

The HDS reaction of DBT was carried out in a Parr model 4522 high-pressure batch reactor. 1.0 g of the catalyst and 150 mL of the freshly prepared solution of DBT in decaline (5% wt/wt, $[DBT]_0 = 0.2388$ mol/L) was introduced in the reactor. The reactor was purged and pressurized to 1.1 MPa with hydrogen and then heated up to 623 K at a rate of 10 K/min under continuous stirring of 600 rpm. After reaching the working temperature and pressure (3.4 MPa), the products were collected for chromatographic analysis every half an hour to determine the conversion-time dependence during 5 h. After the reaction, the used catalysts were filtered, washed and stored in inert atmosphere. The reaction products were analyzed using a Perkin-Elmer Auto-system chromatograph with a 9 ft long × 1/8 inch diameter packed column containing chromosorb W-AW 80/100 mesh 3% OV-17 (phenyl methyl silicone 50% phenyl) as a separating phase.

It is well established that the HDS of DBT occurs by two parallel reactions pathways [15]: (I) direct desulfurization (DDS) via C–S bond cleavage and (II) hydrogenation (HYD). The main products of the HDS reaction are biphenyl (BP, via DDS), cyclohexylbenzene (CHB, via HYD) and tetrahydrodibenzothiophene (TH-DBT, via HYD). The ratio between HYD and DDS can be approximated in terms of the experimental selectivity according to the following equation:

$$\mathrm{HYD/DDS} = ([\mathrm{PCH}] + [\mathrm{TH} - \mathrm{DBT}])/[\mathrm{BP}]$$

The rate constant was determined from the DBT conversion as function of time assuming that DBT conversion being a pseudo-zero order reaction [16] by using of following equation:

$$X_{\mathrm{DBT}} = (1 - \eta\mathrm{DBT})/\eta\mathrm{DBT} = \left(k/\eta_{\mathrm{DBT},\,0}\right)t$$

where X_{DBT} is the fraction conversion of DBT, η_{DBT} = moles of DBT, k = pseudo zero order rate constant, t = time in seconds and $k/\eta_{\mathrm{DBT},\,0}$ is the slope. The mean standard deviation for catalytic measurements was ca. 2.5%.

3 Results

3.1 X-ray Diffraction

In Fig. 1 the low angle diffraction patterns of parent SBA-15 and Ni–MoS_2/SBA-15 catalysts are displayed. The three characteristic reflections (100), (110), and (200) of hexagonal mesoporous SBA-15 (space group $p6$ mm) are observed for all samples giving strong evidence that the primary structure of SBA-15 consisting of well ordered channels is preserved after the incorporation of NiMo sulfides. The decrease of the Bragg reflection intensity after impregnation may be caused by phase cancellation between the pore walls and the guest species, the strong absorption of X-rays by Mo and/or a partial loss of the high order of the mesostructure. This is a well-known phenomenon and was described previously in the literature [6, 8, 10].

Figure 2 illustrates XRD patterns of the SBA-15 supported catalysts in the 2θ range from 7° to 75°. Characteristic reflections of poorly crystalline 2H–MoS_2 appear at 14.4, 33, 40, and 58° 2θ. The typical partial turbostratic disorder [8, 17] of layered MoS_2 leads to the occurrence of the asymmetric shape on the low angle side of the reflections (Fig. 2). The broad peak at about 22° 2θ is caused by the amorphous SBA-15 silica. The average MoS_2 crystal sizes can be estimated with the Scherrer formula, $d = 0.941\lambda/B\cos\theta_B$, where d is the mean diameter of the particle, λ is the wavelength of Cu $K_{\alpha 1}$ (0.154056 nm), θ_B is the angle between the incident beam and the reflecting lattice planes, and B is the width of the diffraction peak (full width at half maximum, FWHM), respectively [8]. From the comparison of the estimated average particle sizes of MoS_2 summarized in Table 1, it is obvious: (1) the sizes of MoS_2 nanoparticles increase with increasing Mo loading; (2) the MoS_2 particle sizes depend on the nature of the precursor used, e.g., the catalyst with the smallest mean MoS_2 crystal size was prepared with TMATM with a Mo loading of 18 wt% (Table 1); (3); larger MoS_2 particles can be observed for the catalysts supported on 9 nm SBA-15 compared to the equivalent samples supported on 6 nm SBA-15; (4) post impregnation with the Ni complex leads to enlarged MoS_2 particle sizes as well as the generation of Ni_3S_2 (Fig. 2g). We want to note that for the Co–MoS_2/SBA-15 catalysts prepared by

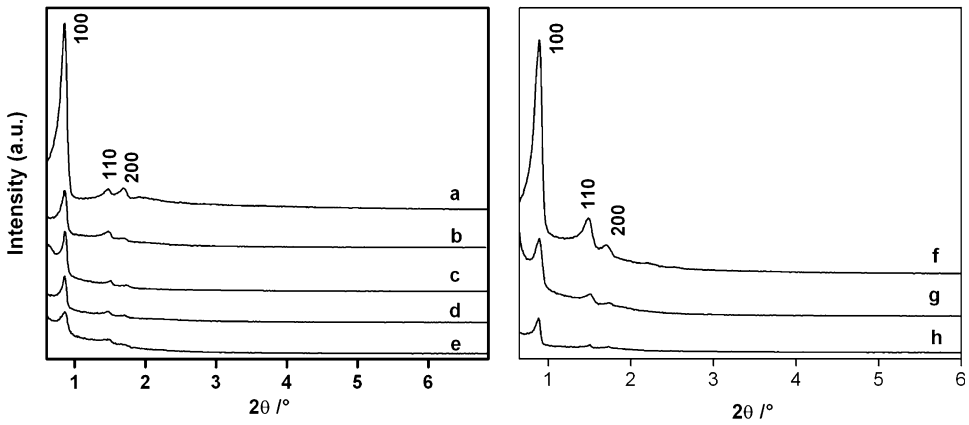

Fig. 1 XRD patterns of (a) parent SBA-15 (6 nm), (b) Ni(1.5)Mo(10)/SBA-15(6A), (c) Ni(2.0)Mo(18)/SBA-15(6B), (d) Ni(1.5)Mo(10)/SBA-15(6C), (e) Ni(4.0)Mo(18)/SBA-15(6C), (f) parent SBA-15 (9 nm), (g) Ni(1.5)Mo(10)/SBA-15(9A), (h), Ni(1.5)Mo(10)/SBA-15(9B)

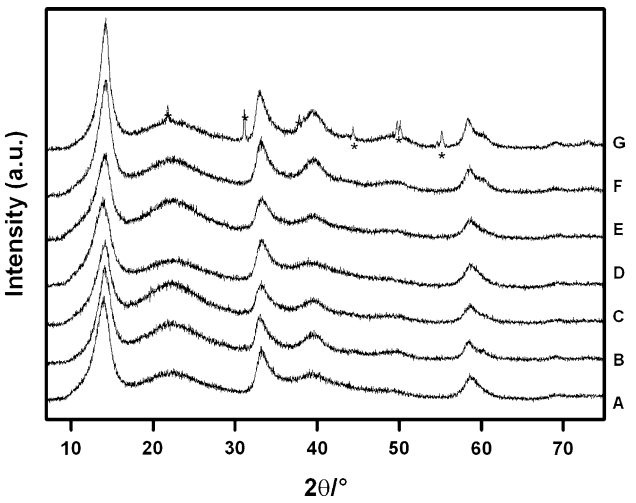

Fig. 2 Wide-angle XRD patterns of A) Ni(1.5)Mo(10)/SBA-15(9B), B) Ni(1.5)Mo(10)/SBA-15(9A), C) Ni(1.5)Mo(10)/SBA-15(6C), D) Ni(2.0)Mo(18)/SBA-15(6B), (E) Ni(1.5)Mo(10)/SBA-15(6A), (F) Ni(2)Mo(18)/SBA-15(6A), (G) Ni(4.0)Mo(18)/SBA-15(6C)

the same methods [9], no crystalline Co sulfide phases could be detected. The presence of Ni_2S_3 particles probably related to the fact that Ni_3S_2 aggregates more rapidly under the synthesis conditions than Co_9S_8 because of its lower Tamman temperature (532 K for Ni_3S_2 versus 686 K for Co_9S_8) [18, 19]. The average MoS_2 particle size is found to be around 4 nm (Table 1) (corresponds to five to six stacking layers along the c-axis), which is a typical MoS_2 size observed for the catalysts supported on SBA-15 prepared with ATM [8, 9]. Comparing the size of MoS_2 nanocrystals with the pore diameters of the SBA-15 material suggests that the MoS_2 crystallites might be located inside the channels of SBA-15.

3.2 Nitrogen Physisorption

The N_2 adsorption–desorption isotherms (at 77 K) of the catalysts are displayed in Fig. 3. All materials show a type IV isotherm which is a typical feature for mesoporous materials. This observation is another evidence that the incorporation of Ni and Mo species does not destroy the mesoporous structure of SBA-15. Table 1 summarizes the (normalized) BET surface areas of the different materials. The specific surface areas show a strong diminution after formation of Ni–Mo sulfides on SBA-15. This phenomenon can be assigned both to the dilution of the support

Table 1 Specific surface area, normalized surface area of SBA-15 support and NiMo sulfide catalysts supported on SBA-15 and the mean MoS_2 crystal size. Normalized (S) = $S_{NiMo}/((1 - wf)\ S_{SBA\text{-}15})$, where S is specific surface area, wf is the weight fraction of NiMo sulfides

Catalysts	Mo wt%	Ni wt%	BET surface area ($m^2\ g^{-1}$)		MoS_2 mean crystal size (nm)
				Normalized	
SBA-15 (6 nm)	0	0	742.2	1	–
Ni(1.5)Mo(10)/SBA-15(6A)	10	1.5	314.7	0.55	3.8
Ni(2.0)Mo(18)/SBA-15(6A)	18	2.0	298.9	0.59	4.3
Ni(2.0)Mo(18)/SBA-15(6B)	18	2.0	232.2	0.48	3.6
Ni(1.5)Mo(10)/SBA-15(6C)	10	1.5	315.9	0.54	3.9
Ni(4.0)Mo(18)/SBA-15(6C)	18	4.0	285.3	0.59	4.8
SBA-15 (9 nm)	0	0	457	1	–
Ni(1.5)Mo(10)/SBA-15(9A)	10	1.5	324.3	0.88	4.3
Ni(1.5)Mo(10)/SBA-15(9B)	10	1.5	312.6	0.85	3.8

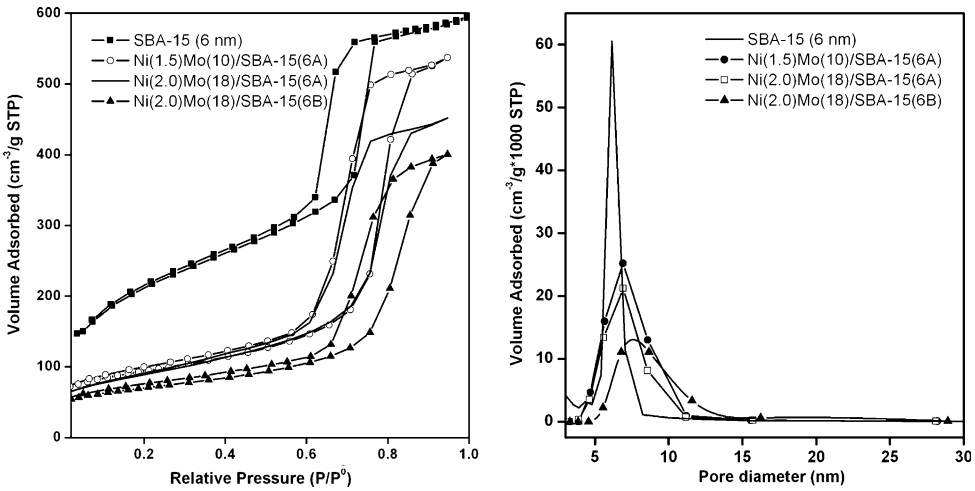

Fig. 3 Nitrogen adsorption/desorption isotherms of Ni–MoS_2/SBA-15 catalysts

by the Mo and Ni compounds and the pore blocking effect generated by NiMo sulfides.

Taking the dilution effect into account the so-called normalized surface areas per weight of silica were calculated according to the procedure given in [20]. Higher normalized surface areas are observed for the Ni–MoS_2/SBA-15 (6 nm) catalysts prepared with ATM compared to the catalysts supported on 6 nm SBA-15 using TMATM as precursor. The two NiMo catalysts supported on 9 nm SBA-15 show similar high normalized surface areas independent of the precursor applied for the preparation (see Table 1). A significant influence on the normalized surface area changes according to the impregnation order can be ruled out (Ni(1.5)Mo(10)/SBA-15(6A) versus Ni(1.5)Mo(10)/SBA-15(6C), Table 1). Furthermore, an increase in the concentration of Ni from 2.0 to 4 wt% yields no changes of the normalized surface areas (see Table 1).

3.3 Transmission Electron Microscopy

The different synthesis methods for the catalysts do not affect the medium-range ordering of the mesoporous SBA-15 host which is fully maintained. For all samples, EDS analyses performed on slabs indicate a Mo : S-ratio close to 0.5 and the presence of Ni inside the slabs, however, the length and stacking number of MoS_2 slabs vary strongly. Samples derived from ATM, e. g. Ni(1.5)Mo(10)/SBA-15(6A), Ni(2.0)Mo(18)/SBA-15(6A), Ni(1.5)Mo(10)/SBA-15(6C) and Ni(4.0)Mo(18)/SBA-15(6C), contain a mixture of short and long MoS_2 slabs with low and high aspect ratios, respectively. Depending on their morphology, the slabs are arranged characteristically on the support particles.

Short slabs with an average stacking number of 4–8 are randomly arranged on the SBA-15 support; see Fig. 4a for a SBA-15 particle close to zone axis [001]. The slabs are imaged with high contrast if located on top of a channel of

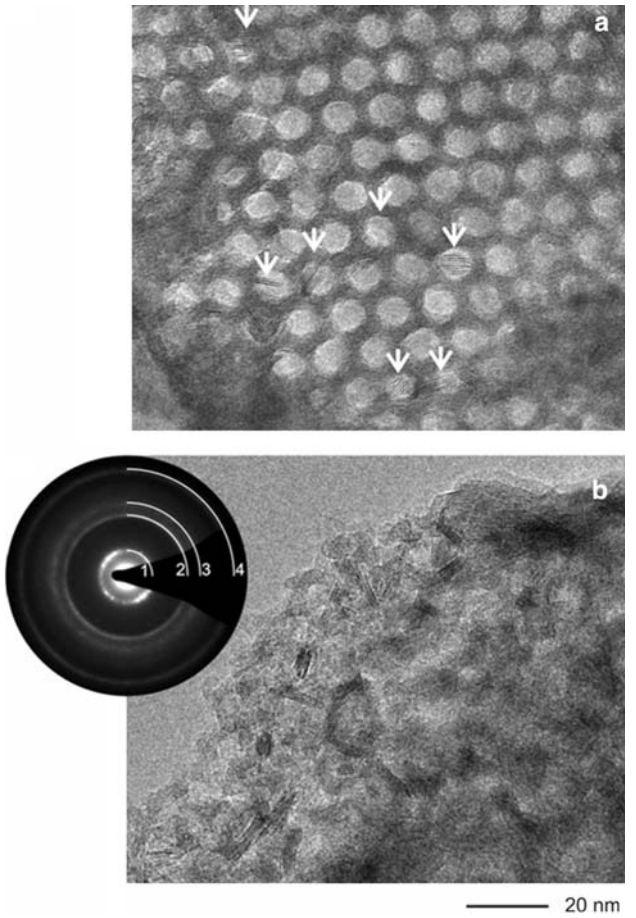

Fig. 4 (**a**) NiMo–Slabs with small aspect ratios (sample Ni(2.0)Mo(18)/SBA-15(6A)) dispersed on a SBA particle, (**b**) aggregation of long slabs at the edge of SBA particles with inserted SAED pattern

the SBA-15 support (see arrows). Fourier transforms of high resolution micrographs as well as the corresponding electron diffraction patterns contain diffuse and homogeneously distributed intensity on concentric rings around

000. The diameters of the rings correlate well those calculated for MoS_2 [21]. e.g. 1: d(002) = 6.2 Å (calc.: 6.16), 2: d(100) = 2.7 Å (calc. 2.74 Å), 3: d(103) = 2.3 Å (calc. 2.28 Å) and 4: d(110) = 1.6 Å (calc. 1.58 Å), cf. Fig. 4b. Thick slabs with an aspect ratio larger than 8 are bent and aggregate preferably at the edges of the SBA-15 particles (see Fig. 4b). When transmitting such areas, the SAED patterns (inset in Fig. 4b), show concentrations of the diffuse intensity inside the concentric rings due to the increase of the thickness and aspect ratios of the slabs.

The Ni content of thin and thick slabs varies not significantly and is restricted to traces; hence, the actual impregnation techniques do not increase the Ni content inside the slabs. This finding could stem from a preferred formation of Ni-rich byproducts which were actually observed in the form of amorphous and crystalline Ni sulfides. Their composition can not reliably be quantified by EDS due to an intergrowth and superposition of the byproducts with MoS_2 slabs. The section of an amorphous particle in Fig. 5a shows parallel stripes at the border area. The repeat unit of consecutive stripes as deduced from Fourier transforms and contrast line profiles are consistent with a repeat unit of consecutive MoS_2 slabs according to d(002) $\sim$ 6.2 Å. EDS scans at the border areas substantiate an enhancement of Mo–K–, (Mo–L, S–K)-peaks and electron diffraction display the characteristic circles of intensity expected for MoS_2 slabs. Consequently one can conclude that the particles are enveloped by MoS_2 slabs.

Moreover, large faceted and fully crystalline Ni sulfides were observed. Like the amorphous particles, the crystallites are enveloped by MoS_2 slabs, cf. stripes in the bright-field image of Fig. 5c. For the identification of the crystalline Ni–S phase, the quasi kinematical intensity inside precession electron diffraction patterns [22–26] was analyzed. The experimental pattern of Fig. 5b (left) is well approximated by the simulation (Fig. 5b, right) when assuming the structure of Ni_3S_2 (Heazlewoodite, [27]), zone axis [122] for the calculation. In particular, the aberration from fourfold intensity distribution and slight, but characteristic deviations from rectangularity of the metrics are well reproduced ($\angle([01-1]^*, [-111]^* = 88.8°$). The experimental pattern also shows the concentric rings of diffuse intensity concentrations originating from the MoS_2 slabs surrounding the crystal (see the arrow highlighting the circle with diameter d(002) $\sim$ 6.2 Å). Inhomogeneous nanostructures based on a core and MoS_2 shells were frequently observed in the past, even for NiS–MoS_2 core-shell particles [28, 29]. Recently, Ni sulfide segregation decorated with MoS_2 layers were also observed in Type 1/2 Ni–Mo catalysts by TEM [19]. Furthermore, composites with suboxide (MoO_{3-x}) core represent intermediates in the formation of hollow MoS_2 nano-onions [30], however, the

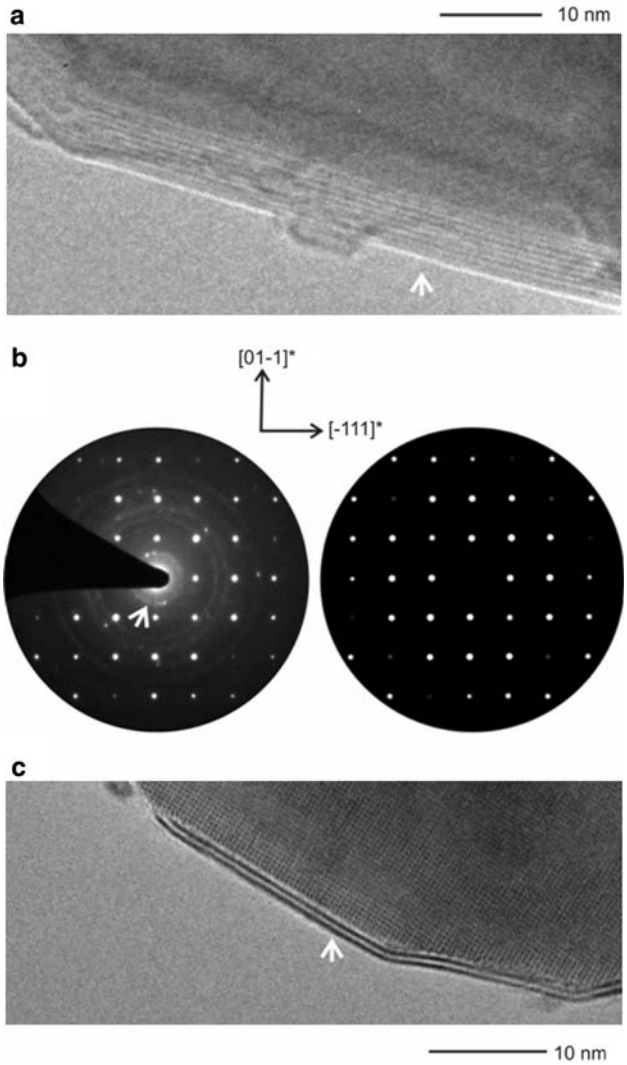

Fig. 5 (**a**) Border area of an amorphous Ni-sulfide with thick coating by MoS_2 slabs, see arrow. (**b**) Experimental PED pattern (left) and simulation (right, based on Ni_3S_2, zone axis [211]). (**c**) Crystallite of Ni_3S_2 with thin coating by MoS_2 slabs, see arrow

latter were never observed in the samples under consideration.

Sample Ni(2.0)Mo(18)/SBA-15(6B) obtained from TMATM exhibits considerable differences in the morphology of the NiMo components. A minor fraction of NiMo slabs was restricted to the thick species with a high aspect ratio. In contrast to all other investigated samples, NiMo nano-onions [30–32] located outside the SBA-15 pore system were identified as the main component, which are seen in the bright-field image in Fig. 6a and high-resolution micrograph of Fig. 7 (left). The EDS mapping in Fig. 6c clearly shows the presence of Mo and S inside the nano-onions, and EDS performed in the nanoprobe mode point to an atomic ratio Mo : S close to 0.5 and evidence traces of Ni. Hence, the nano-onions are composed of bent

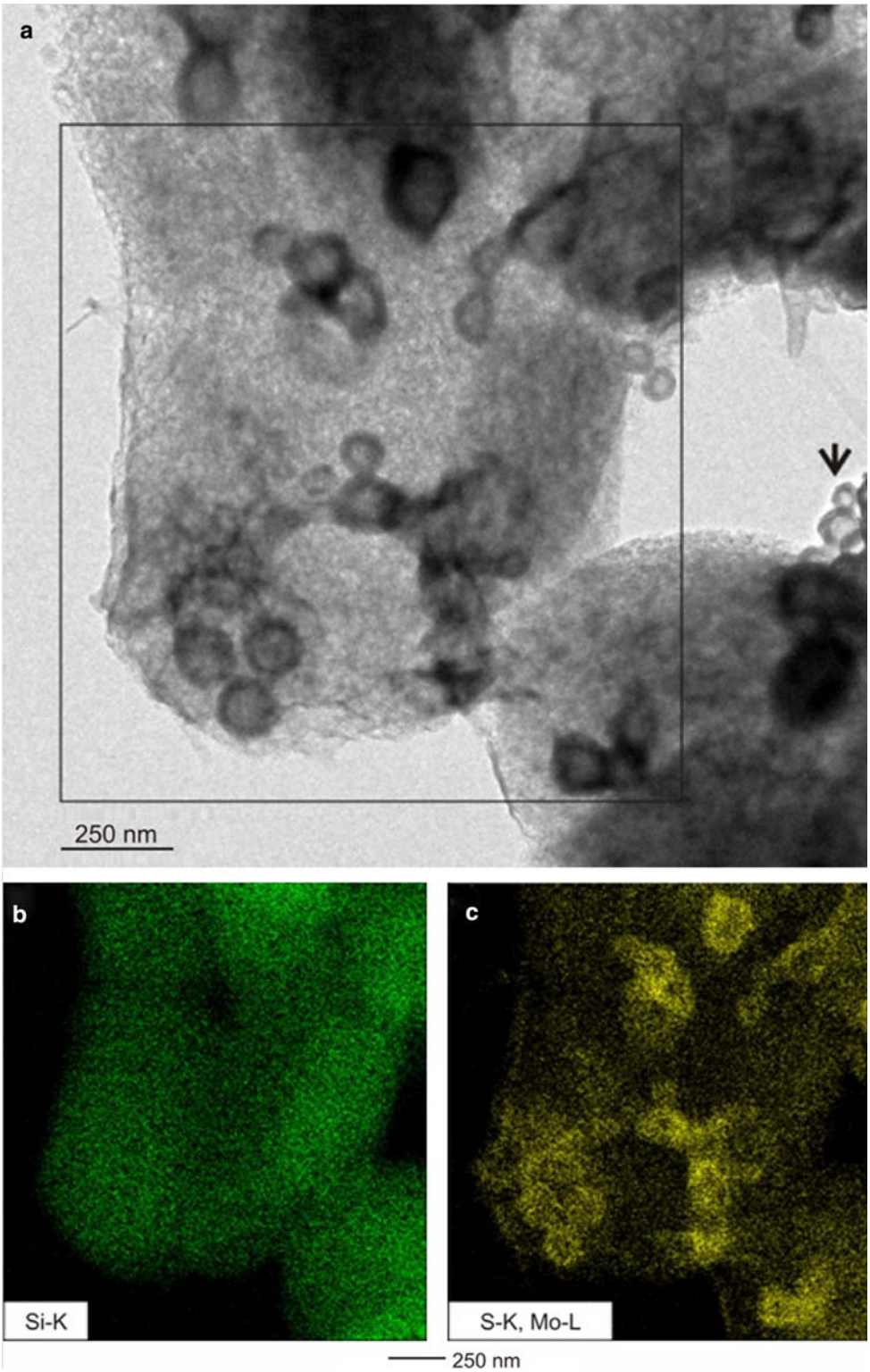

Fig. 6 (**a**) Bright-field image recorded on a SBA particle of sample Ni(2.0)Mo(18)/SBA-15(6B). EDS mapping based on the peaks of (**b**) Si–K, and (**c**) S–K, Mo–L

(Mo,Ni)S_2 layers. Their initial crystalline perfection is low and dominated by defects which were described as intrinsic feature particularly of nano-onions with the thickness exceeding a critical value [33].

The SAED pattern of Fig. 7 (right) was recorded on a single nano-onion. Again, the circles correlate with the metrics of MoS_2 slabs, but due to the low crystallinity, the width of the circles appears broad compared to the one of

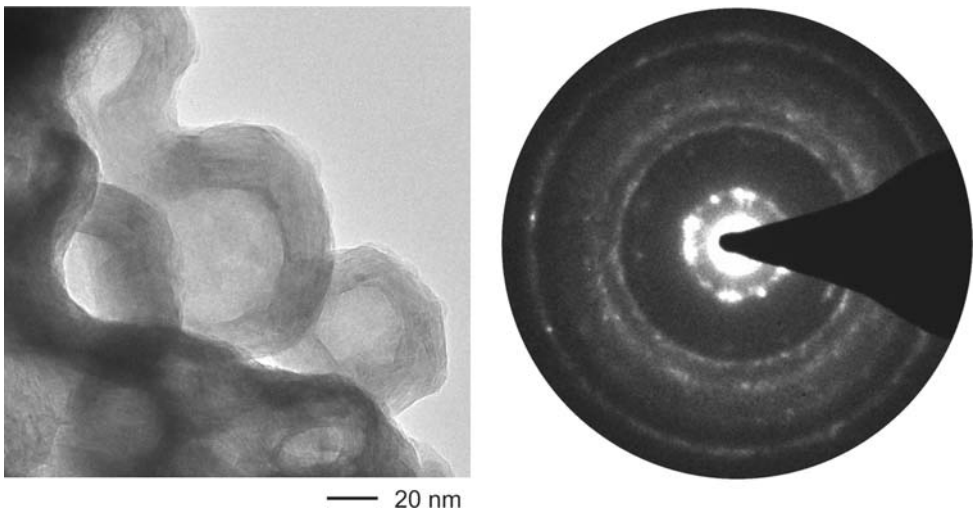

Fig. 7 High-resolution micrograph of MoS_2 onions (cp. arrow in Fig. 6) with intergrowth and attached SAED pattern, Nano-onions before (left) and after (right) extended times or irradiation

crystalline MoS_2 slabs. Accordingly, the bright field image of Fig. 7 (left) shows no clear stripes corresponding with MoS_2 slabs at the walls of the nano-onions. However, extended times of electron beam irradiation with the dose usually applied for HRTEM significantly increase the crystalline quality and the faceting of the initially round onions. Such effect could be based on the local heating of the nano-onions and the corresponding increase of defect healing. The structural and morphological changes depend on the dose. When removing the condenser aperture the dose can be enhanced by a factor of 40 with respect to the setting of HRTEM. In that case, EDX analyses evidence that the MoNi-nano-onions are at least partially reduced to MoS_{2-x}, and finally the metals (Mo and Ni) are formed after long-term irradiation.

Like the corresponding dichalcogenide nanotubes, MoS_2 nano-onions exhibit a high potential for a plethora of applications [34, 35] For the catalytic activity examined in this work the closed shell structures appear unfavorable as one can expect a low edge versus basal surface activity.

3.4 Catalytic Activity and Selectivity

The molar concentration of DBT as a function of reaction time for the catalysts is depicted in Fig. 8. From the approximate linear relationship between conversion of DBT and time (pseudo-zero order kinetics) the initial rate constants were determined. The obtained rate constants and the selectivities calculated at the DBT conversion of ca. 20% are summarized in Table 2. An increasing Mo loading yields an enhanced rate constant, for example, by increasing the Mo content from 10 to 18 wt%, the rate constant increases from 8.1 to 12.3 $\times$ 10^{-7} mol/gs. This observation is similar to the results achieved for Co–MoS_2/SBA-15 catalysts [8, 9]. Comparison of the rate constants determined for Ni(1.5)Mo(10)/SBA-15(6A) (8.1 $\times$ 10^{-7} mol/g.s) and

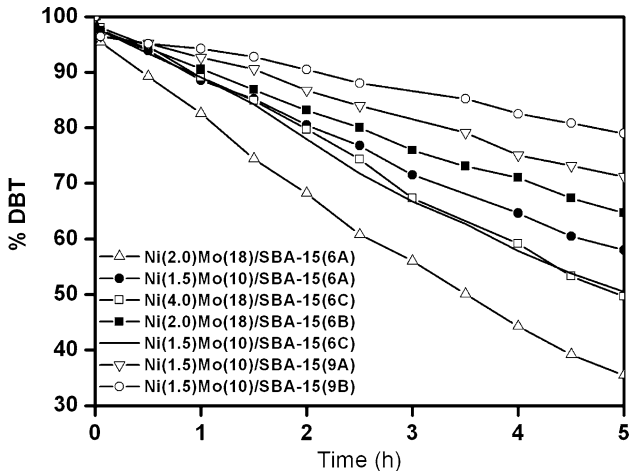

Fig. 8 DBT conversion as function of reaction time for the Ni–MoS_2/SBA-15 catalysts

Ni(1.5)Mo(10)/SBA-15(6C) (9.8 $\times$ 10^{-7} mol/g.s) shows that the impregnation order has nearly no influence on the activity. Interestingly, the increase of Ni concentration by post-impregnation results in a decrease in the HDS activity.

For the same metal loading, Ni–MoS_2/SBA-15(9 nm) catalysts have a significantly lower HDS activity compared with Ni–MoS_2/SBA-15(6 nm). Catalysts prepared with TMATM have a lower rate constant than those synthesized with ATM when the SBA-15 support with same pore size is employed, which suggests the great influence of the thiomolybdate complex on the HDS catalytic activity. We note that the catalyst Ni(1.5)Mo(18)/SBA-15(6A) has a similar activity like a commercial catalysts (NiMo/γ–Al_2O_3) which was characterized under the actual experimental conditions (k = 12 $\times$ 10^{-7} mol/g.s, HYD/DDS = 0.53) [17]. In addition, the HYD/DDS ratios for the present catalysts display a higher selectivity for HYD compared to NiMo/γ–Al_2O_3.

Table 2 Initial rate constants (k) and selectivity HYD/DDS (achieved at a DBT conversion of ca. 20 %) of the Ni–MoS_2/SBA-15 catalysts and a commercial NiMo/γ–Al_2O_3 during the HDS reaction of DBT ($T = 623$ K, $P_{H2} = 3.4$ MPa)

Catalysts	k (specific) (1×10^{-7} mol/gs)	HYD/DDS ratio
Ni(1.5)Mo(10)/SBA-15(6A)	8.1	0.79
Ni(2.0)Mo(18)/SBA-15(6A)	12.3	1.01
Ni(2.0)Mo(18)/SBA-15(6B)	6.6	0.56
Ni(1.5)Mo(10)/SBA-15(6C)	9.8	0.89
Ni(4.0)Mo(18)/SBA-15(6C)	10.0	0.83
Ni(1.5)Mo(10)/SBA-15(9A)	5.4	0.79
Ni(1.5)Mo(10)/SBA-15(9B)	3.6	0.62
NiMo/γ–Al_2O_3	12.0	0.53

4 Discussion

The synthesis method using only thiosalts as starting materials yields supported catalysts with an average MoS_2 stacking of 4–8 layers (see XRD and HRTEM). Despite the presence of pronounced MoS_2 stacking the Ni–MoS_2/SBA-15 catalyst (Ni(2.0)Mo(18)/SBA-15(A), $k = 12.3 \times 10^{-7}$ mol/g.s) reveals a comparable activity with a commercial NiMo/γ–Al_2O_3 catalyst. In line with the previous studies [8, 9] [19] [36] the type of the precursor and the actual synthesis conditions seem to be more important for the generation of catalytic active materials. According to the results published by Eijsbouts et al., the MoS_2 stacking is not a prerequisite for a good HDS performance and also not a sign of deactivation or lower HDS activity [19]. One should note that the rigorous study of Eijsbouts et al. was done on unsupported liquid-phase-sulfided Type 2 commercial ULSD catalysts [19]. A large amount of coordinatively unsaturated sites (CUS) which preferably generated in the reductive atmosphere during the thermal decomposition of ammonium thiomolybdate [8] or ammonium thiotungstate [37] might be responsible for the observed similar high activity compared to the optimized commercial NiMo/γ–Al_2O_3 catalyst.

The Co–MoS_2/SBA-15 catalysts with similar Mo loading prepared with the same synthesis route exhibit apparently higher HDS activity [9] ($k = 15.2 \times 10^{-7}$ mol/g.s). This different HDS performance could to due to the different behavior of promotion with Ni or Co. In the case of NiMo sulfide catalysts, it is generally agreed that the promoting effect of Ni is due to an increased mobility of sulfur in the so-called "Ni–Mo–S" phase, in which Ni is present in a square–pyramidial-like structure [38]. Because a S atom in the Ni–S–Mo linkage is less strong bonded than a S atom between two Mo atoms, it can be removed easily to create catalytic active sites like vacancies or CUS. The amorphous and crystalline Ni sulfides enveloped by MoS_2 slabs can be easily detected in the present Ni–MoS_2/SBA-15 catalysts (see Fig. 5), whereas Co-rich particles in the Co–MoS_2/SBA-15 catalysts [9] could not be detected. This observation is similar to a previous study where the Co sulfides were amorphous but Ni sulfides appear crystalline [19]. According to the "Remote Control" model segregated crystalline Ni_3S_2 may positively contribute to the catalytic performance [39]. Furthermore, increasing the Ni concentration by post-impregnation with NiDETC leads to a significant generation of large faceted Ni_3S_2 crystals (XRD and TEM). The less active Ni_3S_2 might cover the surface of the Ni–Mo–S active phase resulting in a decrease of the HDS activity of DBT (Ni(4)Mo(18)/SBA-15(6C) versus Ni(2)Mo(18)/SBA-15(6C), see Table 2).

The catalyst obtained from TMATM (Ni(2)Mo(18)/SBA-15(6B)) shows the lowest activity of all catalysts supported on 6 nm SBA-15. It seems that the more pronounced pore blocking is responsible for the low HDS activity. A partial blocking of the pore entrance may lead to a decrease in accessibility of the reactants to the active sites [40, 41]. However, the catalysts supported on 9 nm SBA-15 prepared with ATM present obviously higher HDS activity than the catalyst obtained with TMATM despite the similar pore blocking for both samples (Table 2). To explain this result one should also consider the different behaviour of the two precursors during the thermal decomposition reaction. The lower activities for Ni–MoS_2/SBA(9 nm) compared to that of Ni–MoS_2/SBA-15(6 nm) catalysts with the same metal loading can be related to the poor dispersion of the MoS_2 phase (Table 1). SBA-15 with higher specific surface area and smaller pore size seem to be more beneficial for the generation of highly dispersed MoS_2 particles.

The decomposition paths of the different complexes could also be one of the causes for the low HDS activity of the TMATM based catalysts. TMATM decomposes directly to MoS_2 [12], whereas decomposition of ATM proceeds via intermediate formed MoS_3 to MoS_2. It was suggested that amorphous MoS_3 plays an important role in the formation of the active phase in activated carbon-supported systems [42]. In the case of Ni–MoS_2/SBA-15(A), NiDETC is decomposed simultaneously during the generation of MoS_2 from ATM (MoS_3 to MoS_2) and Ni–MoS_2/SBA-15(C) was prepared by post impregnation of (Ni)MoS_2/SBA-15 with NiDETC. It should be noted that both synthesis methods have similar effects on the surface areas of the SBA-15 support (Table 1). At the same Mo and Ni loading, the Ni(1.5)Mo(10)/SBA-15(6C) catalyst shows a slightly higher activity than Ni(1.5)Mo(10)/SBA-15(6A) indicating that the intermediate MoS_3 is not a prerequisite for the generation of HDS active phases under the actual synthesis conditions. This result confirms the previous observation achieved for Co–MoS_2/SBA-15 catalysts [9].

Very recently the atomic-scale structures of Co or Ni promoted MoS_2 nanocluster was studied with STM and density functional theory [43]. According to this study Co promoted MoS_2 particles have a hexagonal shape and Co atoms prefer ($\bar{1}010$) edges with a 50% S coverage. For Ni promoted MoS_2 a size dependence of the morphologies and the Ni sites was observed. Larger particles are very similar to the Co promoted particles, but smaller clusters adopt dodecagonal shapes with three different edges. All edges contain Ni atoms which fully or partially substitute the Mo atoms. Interestingly, in the present work a strong influence of the precursor type onto the MoS_2 morphology is observed in HRTEM micrographs. Whereas mainly MoS_2 slabs are formed for the catalysts derived from ATM, the catalysts prepared with TMATM appear as nano-onions composed of bent MoS_2 layers with low initial crystalline perfection located outside the pores of the SBA-15 support (compare Figs. 4 and 6). In the literature it was proposed that the MoS_2 dispersion and particularly the dispersion of edge and corner Mo atoms plays an important role for the catalytic activity [44], whereas the basal plane of MoS_2 is catalytically not active [45]. A decrease of the average MoS_2 slab length causes an increase in MoS_2 edge and corner atom dispersion, resulting consequently in an increase of the catalyst activity for HDN of heavy gas oil derived from Athabasca bitumen [46]. The closed shell structure of MoS_2 nano-onions offers a low amount of the HDS active edge sites. One can conclude that the MoS_2 morphologies observed in the HRTEM pictures for the catalysts prepared with TMATM are mainly responsible for the low HDS activity.

The detailed analysis of the reaction product distributions at the same total DBT conversion (20%, Table 2) demonstrates that for all NiMo catalysts with exception of Ni(2)Mo(18)/SBA-15(A) the DDS pathway is slightly preferred, which is a typical promoting effect of Ni. The higher HYD activity compared to the Co–MoS_2/SBA-15 catalysts prepared applying the same method (HYD/DDS = ca. 0.2 [9]) suggests that the active site for HYD is distinct from that for DDS, which is in good agreement with the previous studies [47, 48]. Moreover, the Ni–MoS_2/SBA-15 catalysts prepared from ATM exhibit larger HYD/DDS ratios (0.79–1.01) compared to the ratio for the above-mentioned commercial NiMo/γ–Al_2O_3 catalyst (0.53). We note that similar HYD/DDS ratios were also observed by Alonso et al. for NiMo sulfide catalysts [49]. Unfortunately, no HRTEM images were published so that a comparison with the morphology of the MoS_2 phase in the present work is not possible. HRTEM characterization was performed by Klimova et al. [50] for NiMo sulfide catalysts supported on MCM-41 and on P modified MCM-41. On the pure silica MCM-41 MoS_2 crystallites exhibit lengths between 30 and 60 Å and two to four stacked layers. With a low amount of P the length of the MoS_2 particles decreases and two to three MoS_2 layers were observed. The increased preference for HYD route products after the incorporation of P atoms was attributed to the changes of the morphology of the active phase. For the present catalysts it can be assumed that the higher HYD activity is also related to the morphology of the Ni promoted MoS_2 crystallites. Thicker MoS_2 slabs provide a larger number of vacancies or CUS compared with single-layered or thin slabs. The π-complexation of the aromatic ring on such thick MoS_2 slabs is then easier compared to single-layered or thin slabs [50] and consequently results in higher HYD activity.

5 Conclusions

In this study, Ni promoted MoS_2 catalysts dispersed on SBA-15 as support were prepared from sulfur-containing Mo and Ni complexes. The results achieved from XRD, N_2 physisorption, HRTEM and the HDS catalytic activity of DBT lead to the following conclusions:

1. One catalyst obtained with ATM as precursor shows a similar high catalytic activity like a NiMo/γ–Al_2O_3 catalyst despite the presence of large stacking number of MoS_2 layers. This observation may be explained by the presence of a large amount of vacancies (CUS) created during the thermal decomposition of ATM in a H_2/N_2 atmosphere.
2. The formation of crystalline Ni sulfides enveloped by MoS_2 slabs is apparently observed in the Ni–MoS_2/SBA-15 catalysts. The enhancement of the Ni content by post-impregnation leads to the formation of segregated Ni_3S_2 particles, which can cover the surface of the Ni–Mo–S phase resulting in a decrease of the HDS activity.
3. The precursor type has a stronger influence onto the MoS_2 morphology than the impregnation method. The generation of nano-onions composed of bent MoS_2 layers with a low crystalline perfection derived from TMATM could be the main factor for the low observed HDS activity.
4. The multilayered nature of the Ni–MoS_2 phase may be responsible for the higher HYD/DDS ratios (0.79–1.01) for the Ni–MoS_2/SBA-15 catalysts prepared from ATM compared to the ratio for the commercial NiMo/γ–Al_2O_3 catalyst (HYD/DDS = 0.53).

Acknowledgments The authors thank V. Duppel for practical TEM work, Prof. A. Simon for enabling the TEM experiments. Financial support by the Deutsche Forschungsgemeinschaft (DFG, grant BE 1653/22-1)

References

1. Zhao D, Feng J, Huo Q, Melosh N, Fredrickson GH, Chmelka BF, Stucky GD (1998) Science 279:548
2. Vradman L, Landau MV, Herskowitz M, Ezersky V, Talianker M, Nikitenko S, Koltypin Y, Gedanken A (2003) J Catal 213:163
3. Dhar GM, Kumaran GM, Kumar M, Rawat KS, Sharma LD, Raju BD, Rao KSR (2005) Catal Today 99:309
4. Klimova T, Lizama L, Amezcua JC, Roquero P, Terrés E, Navarrete J, Domínguez JM (2004) Catal Today 98:141
5. Kumaran GM, Garg S, Soni K, Kumar M, Sharma LD, Dhar GM, Rao KSR (2006) Appl Catal A Gen 305:123
6. Gutiérrez OY, Fuentes GA, Salcedo C, Klimova T (2006) Catal Today 116:485
7. Gutiérrez OY, Valencia D, Fuentes GA, Klimova T (2007) J Catal 249:138
8. Huang Z-D, Bensch W, Kienle L, Fuentes S, Alonso G, Ornelas C (2008) Cat Lett 122:57
9. Huang Z-D, Bensch W, Kienle L, Fuentes S, Alonso G, Ornelas C (2008) Cat Lett (Submitted)
10. Huang Z-D, Bensch W, Sigle W, van Aken PA, Kienle L, Vitova T, Modrow H, Ressler T (2008) J Mater Sci 43:244
11. Brieler FJ, Grundmann P, Fröba M, Chen LM, Klar PJ, Heimbrodt W, von Nidda HAK, Kurz T, Loidl A (2004) J Am Chem Soc 126:797
12. Poisot M, Bensch W, Fuentes S, Alonso G (2006) Thermochim Acta 444:35
13. Jorgensen CK (1962) J Inorg Nucl Chem 24:1571
14. E. 1.0, AnaliTEX (2002–2007) Stockholm, Sweden
15. Whitehurst DD, Isoda T, Mochida I (1998) Adv Catal 42:345
16. Candia R, Clausen BS, TopsØe H (1982) J Catal 77:564
17. Poisot M, Bensch W, Fuentes S, Ornelas C, Alonso G (2007) Cat Lett 117:43
18. Zhao XJ, Wei J (1994) J Catal 147:429
19. Eijsbouts S, van den Oetelaar LCA, van Puijenbroek RR (2005) J Catal 229:352
20. Landau MV, Vradman L, Herskowitz M, Koltypin Y, Gedanken A (2001) J Catal 201:22
21. Petkov V, Billinge SJL, Larson P, Mahanti SD, Vogt T, Rangan KK, Kanatzidis MG (2002) Phy Rev B 65:092105
22. Vincent R, Midgley PA (1994) Ultramicroscopy 53:271
23. Gjonnes J, Hansen V, Krerneland A (2004) Microsc Microanal 10:16
24. Weirich TE, Portillo J, Cox G, Hibst H, Nicolopoulos S (2006) Ultramicroscopy 106:164
25. Gemmi M, Zou X, Hovmoller S, Migliori A, Vennstrom M, Andersson Y (2003) Acta Cryst A59:117
26. Own C (2005) Northwestern University Evanston Illinois
27. Fjellvag H, Andersen A (1994) Acta Chem Scand 48:290
28. Sanders JV (1986) Ultramicroscopy 20:33
29. Sanders JV (1986) J Electr Micr Techn 3:67
30. Tenne R, Margulis L, Genut M, Hodes G (1992) Nature 360:444
31. Margulis L, Salitra G, Talianker M, Tenne R (1993) Nature 365:113
32. Feldman Y, Wasserman E, Srolovitz DJ, Tenne R (1995) Science 267:222
33. Srolovitz DJ, Safran SA, Homyonfer M, Tenne R (1995) Phys Rev Lett 74:1779
34. Bar-Sadan M, Kaplan-Ashiri I, Tenne R (2007) Eur Phys J 149:71 Special Toppics
35. Camacho-Bragado GA, Elechiguerra JL, Olivas A, Fuentes S, Galvan D, Yacaman MJ (2005) J Catal 234:182
36. Lauritsen JV, Bollinger MV, Lægsgaard E, Jacobsen KW, Nørskov JK, Clausen BS, Topsøe H, Besenbacher F (2004) J Catal 221:510
37. Wilkinson K, Merchan MD, Vasudevan PT (1997) J Catal 171:325
38. Qian WH, Hachiya Y, Wang DH, Hirabayashi K, Ishihara A, Kabe T, Okazaki H, Adachi M (2002) Appl Catal A Gen 227:19
39. Karroua M, Matralis H, Grange P, Delmon B (1993) J Catal 139:371
40. Furimsky E, Massoth FE (1993) Catal Today 17:535
41. Absihalabi M, Stanislaus A, Trimm DL (1991) Appl Catal 72:193
42. Brito JL, Severino F, Delgado NN, Laine J (1998) Appl Catal A Gen 173:193
43. Lauritsen JV, Kibsgaard J, Olesen GH, Moses PG, Hinnemann B, Helveg S, NØrskov JK, Clausen BS, TopsØe H, Lægsgaard E, Besenbacher F (2007) J Catal 249:218
44. Hensen EJM, Kooyman PJ, van der Meer Y, van der Kraan AM, de Beer VHJ, van Veen JAR, van Santen RA (2001) J Catal 199:224
45. Kasztelan S (1990) Langmuir 6:590
46. Ferdous D, Dalai AK, Adjaye J, Kotlyar L (2005) Appl Catal A Gen 294:80
47. Cristol S, Paul JF, Payen E, Bougeard D, Hutschka F, Clémendot S (2004) J Catal 224:138
48. Egorova M, Prins R (2006) J Catal 241:162
49. Alonso G,Chianelli RR,Fuentes S, Torres B (2007) U.S. Patent
50. Herrera JM, Reyes J, Roquero P, Klimova T (2005) Micropor Mesopor Mater 83:283